

# The High Resolution *IRAS* Galaxy Atlas

Yu Cao

Division of Physics, Mathematics, and Astronomy, California Institute of Technology,  
Pasadena, California 91125

Susan Terebey

Extrasolar Research Corporation and California Institute of Technology,  
Pasadena, California 91125

Thomas A. Prince

Division of Physics, Mathematics, and Astronomy, California Institute of Technology,  
Pasadena, California 91125

Charles A. Beichman

Infrared Processing and Analysis Center, California Institute of Technology,  
Pasadena, California 91125

## ABSTRACT

An atlas of the Galactic plane ( $-4.7^\circ < b < 4.7^\circ$ ) plus the molecular clouds in Orion,  $\rho$  Ophiuchus, and Taurus-Auriga has been produced at 60 and 100  $\mu\text{m}$  from *IRAS* data, with  $1' - 2'$  resolution. The *IRAS* Galaxy Atlas, together with the DRAO HI line / 21 cm continuum and FCRAO CO (1-0) line Galactic plane surveys, both with similar ( $\sim 1'$ ) resolution, provide a powerful venue for studying the interstellar medium, star formation and large scale structure in our Galaxy. This paper documents the production and characteristics of the Atlas.

## 1. Introduction

In 1983 the *Infrared Astronomical Satellite* fundamentally changed our view of the infrared sky when it conducted the first infrared all sky survey. The *IRAS* data have proven important to the study of many astrophysical phenomena including star formation, the interstellar medium, Galactic structure, late-type stars, supernova remnants, external galaxies, infrared cirrus, and debris disks around nearby stars (Beichman review ref). New infrared spacecraft missions such as ISO, MSX, and IRTS now provide higher sensitivity and spatial resolution. However by design they cover only a small fraction of the sky, thus ensuring that *IRAS* will provide a fundamental archive for many years to come.

The native spatial resolution of the *IRAS* coadded data is a few by five arcminutes. Various image reconstruction techniques have been applied to the *IRAS* data in the quest to extract higher spatial resolution (Terebey & Mazzarella 1994). These include maximum entropy techniques, among them the HIRAS package developed at Groningen (Assendorp et al. 1995, Bontekoe et al. 1994). Making use of an alternate approach, the production of the *IRAS* Galaxy Atlas is based on the well-known HIRIES processor, first developed in 1991 and made available to the scientific community by the Infrared Processing and Analysis Center (IPAC). HIRIES implements the iterative Maximum Correlation Method (MCM; Aumann, Fowler, & Melnyk 1990), a variant of the Richardson-Lucy algorithm which has been optimized for *IRAS* data. The advantages of HIRIES include flux conservation, speed of processing, and the ability to work reliably on faint sources. HIRIES images have been successfully used for a variety of galactic and extragalactic studies (Rice 1993, Surace et al. 1993, Terebey & Mazzarella 1994).

The parallel supercomputing facilities available at Caltech and the development of new artifact reduction algorithms made possible a large-scale high-resolution *IRAS* mapping of the Galactic plane (Cao et al. 1996, hereafter referred to as Paper I). The new *IRAS* Galaxy Atlas (IGA) maps, which have  $1' - 2'$  resolution, provide a ten-fold improvement in areal resolution over the *IRAS* Sky Survey Atlas (ISSA; Wheelock et al. 1994). The IGA incorporates several important differences from standard HIRIES processing at IPAC. Foremost is improved destriping and zodiacal emission subtraction, which lead to reduced artifacts, enhanced structure, and the ability to mosaic images without edge discontinuities. The IGA is well suited to high-resolution studies of extended structure, and will be valuable for a wide range of scientific studies, including: the structure and dynamics of the interstellar medium (ISM); cloud core surveys within giant molecular clouds; detailed studies of HII regions and star forming regions; determination of initial mass functions (IMFs) of massive stars; and study of supernova remnants (SNRs). The IGA will be especially useful for multi-wavelength studies using the many Galactic plane surveys that have similar ( $\sim 1'$ ) resolution. These include the new FCRAO CO(1-0) spectral line (Heyer 1996) and DRAO HI line / 21 cm continuum surveys (Normandeau, Taylor, & Dewdney 1996).

All image reconstruction algorithms have their quirks. This paper describes and characterizes the IGA so that it will be useful for quantitative scientific study. Section 2 describes the geometry and information content of the atlas images. Section 3 gives a description on the various processing stages, namely the basic algorithm, subtraction of zodiacal emission, and coordinate transform and reprojection. Section 4 discusses the characteristics of the images, including resolution, photometric and positional accuracy, mosaic properties, and calibration. Discussion of image artifacts is given in Section 5.

The IGA images are available upon request from either the authors, IPAC (info@ipac.caltech.edu) or through the NASA National Space Science Data Center (NSSDC). This paper gives references to online resources (mostly in the form of World Wide Web documents) whenever appropriate. The information is accurate as of 1996.

## 2. Description of the Atlas

The atlas consists of images (1st and 20th iteration) and ancillary maps in FITS (Wells, Greisen, & Harten 1981) format covering  $0^\circ \leq l < 360^\circ$ ,  $-4.7^\circ < b < 4.7^\circ$  in the 60 and 100  $\mu\text{m}$  wavelength bands. The 1st iteration images are coadded *IRAS* images with no resolution enhancement. For the fields covering the Galactic plane, the field of view for each image is  $1.4^\circ \times 1.4^\circ$ , on  $1^\circ$  centers in both the galactic longitude and latitude directions, the pixel size is  $15''$ , and Galactic coordinates and Cartesian projection are used. For the molecular cloud (Orion,  $\rho$  Ophiuchus, Taurus-Auriga) fields, the images are  $2.5^\circ \times 2.5^\circ$  on  $2^\circ$  centers, using Equatorial coordinates (B1950) and Cartesian projection.

The 1st iteration images correspond to coadded *IRAS* images at the native *IRAS* resolution of approximately  $2.0' \times 4.7'$  at 60  $\mu\text{m}$  and  $3.8' \times 5.4'$  at 100  $\mu\text{m}$ . After MCM processing to 20 iterations the typical spatial resolution improves to  $1.0' \times 1.7'$  at 60  $\mu\text{m}$  and  $1.7' \times 2.2'$  at 100  $\mu\text{m}$  (see Section 4.1). CAUTION: Note that the images at 60 and 100  $\mu\text{m}$  have inherently different resolutions. Ratio maps should be attempted only after correcting the images to a common resolution.

The images are on the same absolute flux level as the ISSA images, except for a constant AC/DC factor (see Sec. 4.3).

The ancillary maps include the correction factor variance (CFV) map, the photometric noise (PHN) map, coverage (CVG) map, the detector track (DET) map, and the beam sample map (BEM). See Table 1 in Section 3.2 for the quantities they represent and Section 6 for example images. The FWHM.txt text file gives Gaussian beam sizes derived from the corresponding BEM map.

## 3. Description of Processing

For an overview of the HIRES processing developed at IPAC, see [http://www.ipac.caltech.edu/ipac/iras/hires\\_over.html](http://www.ipac.caltech.edu/ipac/iras/hires_over.html). This section emphasizes the unique problems encountered in the *IRAS* Galaxy Atlas production.

### 3.1. Overview of the Production Pipeline

*IRAS* detector data, known as CRDD (Calibrated, Reconstructed Detector Data), grouped in  $7^\circ \times 7^\circ$  plates, reside in the “*Level 1 Archive*” at IPAC. The first step in the pipeline for mass production of HIRES images is to extract data covering a specific field from the archive and then perform calibration and various other preprocessing.

We take the  $7^\circ \times 7^\circ$  preprocessed and calibrated plates and use the algorithm described in Section 3.3 to subtract the zodiacal background emission. This step requires the corresponding ISSA image as supplemental input (SmLAUN in Fig. 1, Section 3.3).

Following the calibration and zodiacal subtraction, the detector files are broken into  $1.4^\circ \times 1.4^\circ$  fields, and reprojected into Galactic coordinates (from equatorial) if required, with field centers separated by 1 degree (BrkDet in Fig. 1, Section 3.4). The factor-of-two overlap is a conservative insurance against discontinuity across field boundaries (see Section 4.7), as local destriping and different flux bias (see Sec. 3.5) will be applied to each small field. The  $1.4^\circ \times 1.4^\circ$  size is also the maximal field size with complete coverage allowed within one Level 1 plate, given the 2 degree redundancy of the plates and arbitrary location and orientation of the small field relative to the Level 1 plate. Figure 2 illustrates the overlapping IGA fields, and the geometry and orientation of the Level 1 plates that determine the allowed IGA field size.

All operations described above are carried out on workstations.

The small field ( $1.4^\circ \times 1.4^\circ$ ) detector files are then processed into HIRES images, which is done on the Intel Paragon supercomputer. The basic algorithm for image reconstruction is described in Section 3.2. For parallelization strategy and details of the destriping algorithm, see Paper I.

### 3.2. The Maximum Correlation Method

Starting from a model of the sky flux distribution, the HIRES MCM algorithm folds the model through the *IRAS* detector responses, compares the result track-by-track<sup>1</sup> to the observed flux, and calculates corrections to the model. One important characteristic is that the standard MCM algorithm conserves flux. The process is taken through about 20 iterations in an arbitrary tradeoff between speed of processing and artifact development

---

<sup>1</sup>Track, also called *leg* or *scanline*, refers to the set of data samples collected consecutively by one detector moving across a given field.

versus spatial resolution. The algorithm yields a resolution of approximately  $1'$  at  $60\ \mu\text{m}$ . This represents an improvement in resolution by as much as a factor of 20 in solid angle over the previous images from the *IRAS* Full Resolution Survey Coadd (FRESCO). We give a brief description of the MCM algorithm following the formalism and notations of Aumann, Fowler, and Melnyk (1990) .

Given an image grid  $f_j$ , with  $n$  pixels  $j = 1, \dots, n$  and  $m$  detector samples (*footprints*) with fluxes  $D_i : i = 1, \dots, m$ , whose centers are contained in the image grid, an image can be constructed iteratively from a zeroth estimate of the image,  $f_j^0 = \text{const.} > 0$  for all  $j$ . In other words the initial guess is a uniform, flat, and positive definite map. For each footprint, a correction factor  $C_i$  is computed as,

$$C_i = D_i / F_i, \quad (1)$$

where

$$F_i = \sum_j r_{ij} f_j, \quad (2)$$

and  $r_{ij}$  is the value of the  $i$ th footprint's response function at image pixels  $f_j$ . Therefore  $F_i$  is the current estimate of the  $i$ th footprint's flux, given image grid  $f_j$ .

A mean correction factor for the  $j$ th image pixel is computed by projecting the correction factor for the footprints into the image domain:

$$c_j = [\sum_i (r_{ij} / \sigma_i^2) C_i] / [\sum_i (r_{ij} / \sigma_i^2)]. \quad (3)$$

The weight attached to the  $i$ th correction factor for the  $j$ th pixel is  $r_{ij} / \sigma_i^2$ , where  $\sigma_i$  is the *a priori* noise assigned to the  $i$ th footprint.

The  $k$ th estimate of the image is computed by

$$f_j^{(k)} = f_j^{(k-1)} c_j. \quad (4)$$

In practice when the footprint noise  $\sigma_i$  is not easily estimated, an equal noise value for all footprints is assumed, and the MCM is identical to the Richardson-Lucy algorithm (Richardson 1972, Lucy 1974).

The process is carried to 20 iterations, after which time noise and artifacts increase limit further resolution enhancement. However, for strong extended sources further iteration is often beneficial (Rice 1993, Hurt & Barsony 1996).

Table 1 shows the quantities represented by the ancillary maps (Aumann, Fowler, & Melnyk 1990). The correction factor variance (CFV) map gives an estimate of level of

convergence at a certain pixel, measuring the agreement of correction factors projected onto it from different detector footprints. The photometric noise (PHN) map signifies the photometric noise at a pixel, propagated from noise in the detector measurements. The coverage (CVG) map is the sum of the response function grids of all footprints within the field. The detector track (DET) map registers the footprint centers and helps visualize the detector scanning pattern. Artifacts due to low coverage may be diagnosed using the coverage maps. The remaining ancillary maps provide diagnostics for other less frequent artifacts.

The effective beam size in HIRES images depends on the response function and sample density in a complicated fashion, and may vary by factors of three over distances of several arcminutes (Fowler & Aumann 1994). In order to estimate the beam size at any given position and to see typical variation over the field, “beam sample maps” (BEM) are provided. These are produced from simulated detector data based on actual coverage geometry, with the simulation scene being a collection of spike sources against a smooth background. An image of the reconstructed spikes (beam sample map) is generated with all the same processing options as the actual image.

For more detailed information on the HIRES ancillary maps, see [http://www.ipac.caltech.edu/ipac/iras/hires\\_maps.html](http://www.ipac.caltech.edu/ipac/iras/hires_maps.html).

### 3.3. Subtraction of Zodiacal Emission

Zodiacal dust emission is a prominent source of diffuse emission in the *IRAS* survey. The zodiacal contribution to the observed surface brightness depends on the amount of interplanetary dust along the particular line-of-sight, an amount which varies with the Earth’s position within the dust cloud. Consequently, the sky brightness of a particular location on the sky, as observed by *IRAS*, changes with time as the Earth moves along its orbit around the Sun. The different zodiacal emission level in different scanlines, if not subtracted, can cause step discontinuities in the images if adjacent patches of sky were observed at different times.

A physical model of the zodiacal foreground emission based on the radiative properties and spatial distribution of the zodiacal dust was developed by Good (1994). The *IRAS* Sky Survey Atlas (ISSA; Wheelock et al. 1994) made use of this model and subtracted the predicted zodiacal emission from the detector data before co-adding them.

However the *IRAS* detector data, which serve as input to the IGA and other *IRAS* image products, still contain zodiacal emission. A preprocessing method has been developed

to bring the raw detector data flux to a common level with the ISSA images, effectively subtracting the zodiacal emission component (Paper I). Nearby ISSA images ( $12.5^\circ \times 12.5^\circ$ ,  $1.5'$  pixels) were reprojected and mosaicked to cover the same field-of-view as a Level 1 plate ( $7^\circ \times 7^\circ$ ,  $1'$  pixels). A set of simulated data is then calculated from the mosaicked image, by running the actual *IRAS* scan pattern through this image,

$$F_i^{\text{ISSA}} = \sum_j r_{ij} f_j^{\text{ISSA}} \quad (5)$$

The difference between these simulated data and the real data is then used to determine the local zodiacal emission

$$D_i^{\text{ZODY}} = \text{median}(D_i - F_i^{\text{ISSA}}) \quad (6)$$

where the median is taken for nearby footprints in the same scanline with a total spatial range of  $1^\circ$ . The zodiacal component is then subtracted

$$D_i^{\text{NEW}} = D_i - D_i^{\text{ZODY}} \quad (7)$$

and the new data output for use in image construction.

Because of the large spatial scale used in Eq. (6), the resulting zodiacal emission flux  $D_i^{\text{ZODY}}$  varies smoothly with a characteristic scale of  $\sim 1^\circ$ . Therefore the zodiacal subtraction process does not interfere with the high spatial frequency information inherent in the raw data, which is needed for the image reconstruction and resolution enhancement.

### 3.4. Coordinate Transform and Reprojection

Each Level 1 plate covers a field of view of  $7^\circ \times 7^\circ$ , using a projection center local to the plate. The positions of detector footprints are stored in equatorial coordinates using Cartesian projection (Greisen & Calabretta 1996; FITS keywords `RA---CAR`, `DEC--CAR`, B1950):

$$\begin{aligned} x &= \phi, \\ y &= \theta, \end{aligned} \quad (8)$$

where  $\theta$  and  $\phi$  are angles in the native coordinate system (Euler angles with respect to local great circles). Each Level 1 plate has its own projection center ( $C$  in Fig. 3).

For the *IRAS* Galaxy Atlas, the Cartesian projection (FITS keywords `GLON-CAR` and `GLAT-CAR`) with reference point at the Galactic center is convenient, in which case  $l$  and  $b$  map linearly to  $x$  and  $y$ .

To transform the equatorial coordinates of footprints stored in the Level 1 archive to Galactic, the following steps are done in BrkDet. For each footprint centered at  $P$ , a unit vector  $OP$  is computed in the equatorial system, using RA and Dec of the projection center  $C$ , and the  $x$  and  $y$  of  $P$  in the Cartesian projection system centered at  $C$ . Then the unit vector is rotated to the Galactic system, and  $l$  and  $b$  are obtained (see Fig. 3).

Coordinates and fluxes of footprints falling in each  $1.4^\circ \times 1.4^\circ$  field of view are grouped together and written out for the final image reconstruction step.

The tilt angle for each scan line, which is necessary for calculating the response function grid during image reconstruction, also needs to be redetermined in the Galactic coordinate system. For a scan line with  $n$  footprints located at  $(x_i, y_i), i = 1, \dots, n$ , this was done by fitting a straight line through the  $x$  and  $y$  values, by minimizing  $\sum_i \Delta_i^2$ , where  $\Delta_i$  is the distance from footprint  $i$  to the line. This gives the estimate for the tilt angle  $\Phi$ , measured relative to the  $x$  axis

$$\Phi = \frac{1}{2} \arctan \frac{2 \sum_i x_i y_i - \bar{x} \bar{y}}{\sum_i x_i^2 - \bar{x}^2 - y_i^2 + \bar{y}^2} \quad (9)$$

where

$$\begin{aligned} \bar{x} &= \sum_i x_i / n \\ \bar{y} &= \sum_i y_i / n. \end{aligned} \quad (10)$$

For the molecular cloud fields (Orion,  $\rho$  Ophiuchus, and Taurus-Auriga), equatorial coordinates were used (FITS keywords RA---CAR and DEC--CAR, B1950), and the Level 1 archive geometry was retained (no reprojection of the footprint data was performed). Each Level 1 plate ( $7^\circ \times 7^\circ$  on  $5^\circ$  centers) was divided into  $3 \times 3$  subfields of  $2.5^\circ \times 2.5^\circ$  each, on  $2^\circ$  centers, with the projection center the same as the Level 1 plate center. Therefore the subfield images belonging to the same Level 1 plate are mosaickable without the need of reprojection, but special care needs to be taken when mosaicking subfields from different Level 1 plates. The use of Cartesian projection for Equatorial coordinates is closest to the native format of the *IRAS* data, but differs from the more commonly used **-SIN** projection by about 0.5 pixel at the edge of a Level 1 plate.

### 3.5. Issues Related to Flux Bias

Because of the nonlinear nature of the MCM algorithm, the resolution achieved by HIRES processing is not invariant under application of an additive *flux bias*:

$$D_i \longrightarrow D_i + F_{\text{BIAS}}. \quad (11)$$



Generally, the closer to zero the data, the higher the resolution obtained. Alternatively, the more iterations, the higher the resolution obtained. To maximize both spatial resolution and throughput a flux bias is usually applied before the image reconstruction step, to bring the data close to zero and to achieve higher resolution at a given iteration. The applied flux bias is however, subtracted from the output image, so that the surface brightness of the output image matches the original data.

For IGA processing, the flux bias is calculated in the BrkDet step, using the negative of the first percentile from the flux histogram in each  $1.4^\circ \times 1.4^\circ$  field. In other words, the first percentile is used as the zero point in subsequent HIRES processing. The detector data having flux below the first percentile are discarded, since negative data are known to cause instabilities in the algorithm.

## 4. Characteristics of the Images

In this section “IGA(1)” denotes the 1st iteration IGA images, and “IGA(20)” the 20th. The resolution, photometric accuracy, positional accuracy, surface brightness accuracy, mosaic property, and residual hysteresis effect of the images are discussed and quantified.

### 4.1. Resolution

The diffraction limit of the *IRAS* 0.6m telescope is  $50''$  and  $84''$  at 60 and 100 microns, respectively. The effective beam of the coadded *IRAS* data is much larger, typically  $2.0' \times 4.7'$  at 60  $\mu\text{m}$  and  $3.8' \times 5.4'$  at 100  $\mu\text{m}$  due to the large and rectangular *IRAS* detectors. The MCM algorithm makes use of the geometric information in the large number of redundant tracks with differing scan angles to extract higher spatial resolution, which in some cases can approach the diffraction limit of the telescope (Rice 1993). The effective beam size in HIRES images depends on the response function and sample density in a complicated fashion. The resolution also depends on the magnitude of the point source relative to the effective background (see also Sec. 3.5).

The effective resolution of a given field can be estimated from the corresponding BEM maps produced from simulated data (also see Sec. 3.2 and Table 1). To generate the BEM maps artificial point sources are added to the smoothed data, which then undergo HIRES processing. Specifically, point sources are identified and removed from IGA(20) image: the image, further smoothed, provides a model background to which regularly spaced ( $12'$ ) point sources are added. The magnitude of the planted point source spikes is

adjusted according to the dynamic range of the IGA(20) image: the pixel intensity is set to  $20 \times (99\% \text{quantile} - 50\% \text{quantile})$  of the IGA image histogram (plus the background). The numerical value of 20 approximately converts the flux from per unit beam to flux per unit pixel. This arbitrary choice of flux is meant to represent a typical point source which is strong enough with respect to the local galactic background to benefit from high-resolution processing. A set of simulated data is then generated from the artificial image, from which the BEM map is reconstructed through HIRES.

A Gaussian profile is fitted to the reconstructed point sources in the BEM maps, and the FWHM along the major and minor axes are taken as the measure for the achieved resolution.

The typical resolution of the IGA(20) images is  $1.0' \times 1.7'$  at  $60 \mu\text{m}$  and  $1.7' \times 2.2'$  at  $100 \mu\text{m}$ , which represents a substantial improvement over the coadded images. Figure 4 demonstrates the dependence of the resolution upon longitude across the Galactic plane. The plotted major and minor axis FWHM were averaged over latitude. Two obvious dips are seen in the major axis curves, both in  $60$  and  $100 \mu\text{m}$ , near  $l = 100^\circ$  and  $l = 280^\circ$ . These two areas in the Galactic plane featured near-perpendicular intersecting scanlines in the *IRAS* survey, and the extra geometric information in the data gives rise to the increased resolution.

To investigate the dependence of resolution on source strength relative to background level, BEM maps were generated for simulated point sources ranging from 1 to 10,000 Jy in strength. The background intensity level of the test field near  $l = 120^\circ$  was  $53.94 \text{ MJy/ster}$  and  $165.05 \text{ MJy/ster}$  at  $60$  and  $100 \mu\text{m}$ , respectively. Integrated over the effective solid angle of the *IRAS* detectors,  $6.25 \times 10^{-7}$  and  $13.54 \times 10^{-7}$  ster, the detector fluxes due to the local background become  $33.7$  and  $223$  Jy, respectively. To find the effective background during HIRES processing, the flux bias value from the FITS header (see Sec 3.5) can be converted from  $\text{W m}^{-2}$  to Jy through division by the conversion factors  $2.58 \times 10^{-14}$  or  $1.00 \times 10^{-14}$  at  $60$  and  $100 \mu\text{m}$ , respectively, and then subtracted from the corresponding local background flux. In this test case, zero flux bias was used, giving simply  $33.7$  and  $223$  Jy for the processing background at  $60$  and  $100 \mu\text{m}$ , respectively, which is the effective local background felt by the point source during HIRES processing.

The results plotted in Figure 5 show that the IGA(20) resolution is at least a factor of two better than the coadded IGA(1) resolution. Also, the resolution significantly improves for point sources stronger than the processing background of  $33.7$  and  $223$  Jy at  $60$  and  $100 \mu\text{m}$ , respectively. Furthermore, when source-to-background contrast reaches about 20, the achieved resolution becomes insensitive to the background. The resolution in other fields/regions should behave in the same qualitative fashion when the local processing

background is computed as above.

Figure 5 shows the additional effect that offset compensation destriping (Paper I, also see Sec. 5.1) gives comparable but slightly poorer resolution than standard HIRES destriping, especially along the major axis (cross scan) direction.

CAUTION: Note that the images at 60 and 100  $\mu\text{m}$  have inherently different resolutions. Ratio maps should be attempted only after correcting the images to a common resolution.

It should also be noted that the actual beams of the IGA images are not Gaussian. The most prominent deviation of the beam from a 2-dimensional Gaussian is due to the ringing artifact (Section 5.2). Rice (1993) gives a detailed account of the HIRES beams.

## 4.2. Photometric Accuracy

To test photometric accuracy thirty-five relatively isolated point sources (with a well-defined background) were selected. All sources have flux  $> 10$  Jy and are spatially unresolved as measured by the Correlation Coefficient (CC) flag in the Point Source Catalog. Fluxes were measured using an aperture photometry program developed at IPAC, in which the median pixel intensity within an annulus (radius  $5' - 7'$ ) centered at the point source position (taken from the PSC) is taken as the background intensity. Two estimates of the point source flux are then made, using the total fluxes within  $5'$  and  $7'$  radius from the PSC position (minus the background intensity  $\times$  the number of pixels). For sources chosen for the photometry test, these two values are usually sufficiently close to each other to indicate a well-defined background level. The average of these two values is taken as the point source flux from the IGA image, and compared against the value from the PSC.

The computed fluxes are given in Table 2, while Table 3 summarizes the statistical correlation between IGA and PSC flux values.

An overall offset (12%) between the IGA(1) and PSC fluxes is seen at 60  $\mu\text{m}$ , which is, however, not present at 100  $\mu\text{m}$  (1%). One possible explanation for the 60  $\mu\text{m}$  offset is the different data calibration used, specifically the hysteresis correction. The IGA and other recent *IRAS* image products are based on the final *IRAS* Pass 3 calibration, described in detail in the ISSA Expl. Suppl. (Wheelock et al. 1994). This calibration includes a hysteresis correction at both 60 and 100  $\mu\text{m}$  (see Sec. 4.8). The PSC however is based on *IRAS* Pass 2 CRDD data, which were corrected after the fact to the Pass 3 calibration. One significant difference is the way in which hysteresis was treated: the PSC applied a

hysteresis correction only at 100  $\mu\text{m}$  (*IRAS* Catalogs and Atlases: Explanatory Supplement 1988). The lack of hysteresis correction at 60  $\mu\text{m}$  for PSC sources, particularly important for the Galactic plane where hysteresis is strongest, provides one explanation for why there is a systematic offset at 60  $\mu\text{m}$ , but not at 100  $\mu\text{m}$ , between the IGA(1) and PSC fluxes.

In addition, Table 3 shows there is a growth in flux from 1st to 20th iteration which is small (2%) for the 60  $\mu\text{m}$  band, but significant (10%) for the 100  $\mu\text{m}$  band. Analysis shows the effect is caused by depression of the background due to the ringing artifact. In the Galactic plane, where the background emission is strong and structured, the largest contributor to the flux uncertainty is the background determination (Fich & Terebey 1996). The total flux within the selected aperture is comprised of the source flux plus a background contribution (background  $\times$  area). For the photometry sample, the ratio of background flux to source flux is 1.8 at 60  $\mu\text{m}$  and 6.7 in the 100  $\mu\text{m}$  band. In addition the background level systematically decreases on average by 1.7% for 60  $\mu\text{m}$ , and 1.8% at 100  $\mu\text{m}$  due to ringing in the  $5' - 7'$  annulus. This leads to an apparent flux increase from 1 to 20 iterations of  $1.8 \times 1.7\% = 3\%$  at 60  $\mu\text{m}$  and  $6.7 \times 1.8\% = 12\%$  in the 100  $\mu\text{m}$  band, which is in good agreement with results of Table 3.

To compensate for the systematically low background levels we recomputed the IGA(20) source fluxes using IGA(1) background levels. The resulting fluxes show no systematic offset (mean of IGA(20)/IGA(1) = 0.99) and better correlation with IGA(1) fluxes (standard deviation = 0.10). This technique of using IGA(1) backgrounds to calculate IGA(20) fluxes is recommended whenever the most stable and accurate photometry is required.

The growth in flux found for IGA point sources is not a universal property of HIRES processing. In a HIRES study of interacting galaxy pairs, Surace et al. (1993) found HIRES fluxes systematically decreased by 20% from iteration = 1 (FRESCO) to iteration = 20, a result they attributed to the small extended nature of the sample. Since the MCM algorithm fundamentally conserves flux, the effect is either due to a systematic increase in the background, or to redistribution of flux outside the photometric aperture. The use of the IGA(1) background to compute the IGA(20) flux is a technique that can help determine the cause of such systematic trends.

Figure 6 plots the dependence of (IGA(20) flux / PSC flux) on the PSC flux. There is no trend with source flux, apart from the previously discussed offsets.

### 4.3. Size Dependent Flux Correction

The estimation of flux for extended sources ( $> 4' - 40'$ ) may involve a size dependent flux correction, also known as the AC/DC correction. The *IRAS* detectors had a dwell-time dependent responsivity change. Hence, the gain changes as a function of source size: at the *IRAS* survey speed of 3.85 arcmin/s, the gains leveled off for structure on the order of  $40'$  in extent. This effect was band-dependent and largest at  $12\ \mu\text{m}$ . Thus, there are two calibrations for the *IRAS* data, the calibration appropriate for point sources, known as the AC calibration, and the calibration appropriate to very extended structure, known as the DC calibration. To bring point source fluxes measured from DC-calibrated products to the AC (same as the PSC) calibration, the fluxes must be divided by 0.78, 0.82, 0.92 and 1.0 at 12, 25, 60 and  $100\ \mu\text{m}$ , respectively. The *IRAS* Galaxy Atlas uses the AC calibration, while the ISSA images are on the DC scale.

Point source fluxes obtained by aperture photometry with appropriate background subtraction on AC calibrated images should be consistent with the PSC. It should be noted that neither calibration is strictly correct for structure on spatial scales intermediate between point sources and  $30'$  in size. Intermediate-scale corrections and uncertainties can be estimated from the plots in the *IRAS* Catalogs and Atlases: Explanatory Supplement (1988).

### 4.4. Calibration Uncertainty

The measurement uncertainty derived from point sources (Table 3) for the IGA(1) images is 11% and 16% at 60 and  $100\ \mu\text{m}$ , respectively. Given the isolated nature of the sources, these uncertainties represent a best case. A better estimate of the measurement uncertainty in more complex regions is given by Terebey & Fich (1996), who find 17% and 18% for the flux measurement uncertainty of at 60 and  $100\ \mu\text{m}$ , respectively, for a sample of outer Galaxy star forming regions.

In some cases systematic instrumental effects also contribute significantly to the flux uncertainty. The *IRAS* calibration for point sources is accurate, albeit affected by residual hysteresis at 60 and  $100\ \mu\text{m}$  in the Galactic plane. As described in the previous section, there is a 12% systematic uncertainty at  $60\ \mu\text{m}$  between the IGA(1) and PSC. At  $100\ \mu\text{m}$  the uncertainty due to residual hysteresis is less than 5% over most of the Galactic plane, but approaches a maximum of 20% near the Galactic center.

For small but extended ( $5' - 20'$ ) sources the situation is complex. The size-dependent flux correction, the so-called AC/DC effect (see Sec. 4.3) is typically about 10% or less.

However the detector response is not well-behaved for bright extended sources: above 100 Jy the *IRAS* Expl. Suppl. quotes uncertainties of 30% at 60  $\mu\text{m}$  and 70% at 100  $\mu\text{m}$  (*IRAS* Catalogs and Atlases: Explanatory Supplement 1988).

Prominent in the IGA is diffuse Galactic emission associated with HI, which varies on a scale of a few degrees. The *IRAS* – COBE comparison gives an indication of the calibration uncertainty. Over angular scales larger than  $10^\circ$  the *IRAS* calibration differs systematically from that of COBE by 13% and 28% at 60 and 100  $\mu\text{m}$ , respectively (Wheelock et al. 1994).

The ISSA survey was used as large scale surface brightness truth table for the IGA. This implies that defects or uncertainties introduced by the ISSA processing extend to the IGA as well (see Sec. 5.4). At 60 and 100  $\mu\text{m}$ , residuals associated with zodiacal emission model can approach 1 – 2 MJy/ster in the ecliptic plane (Galactic center and anti-center directions), but are typically far less (e.g. Fich & Terebey 1996). For more information consult the ISSA Expl. Suppl. (Wheelock et al. 1994).

#### 4.5. Positional Accuracy

*IRAS* Point Source Catalog positions were used as “truth tables” for a positional accuracy test of the *IRAS* Galaxy Atlas.

Positions were computed for the same sample of thirty-five sources used in the photometry comparison. For each source, a circular area with radius  $5'$  was defined (centered at the PSC position), and the area’s flux weighted centroid was taken as the point source position implied by the IGA image and compared against the PSC position.

Table 4 shows the result of the comparison. For the 60  $\mu\text{m}$  band, the distances between the IGA position and PSC position have an average of  $7.6''$  and standard deviation  $5.6''$ , while for 100  $\mu\text{m}$ , there is a  $7.1'' \pm 4.1''$  difference.

The PSC quoted error ellipses corresponding to the 95% confidence level for source positions. The major and minor axes of the error ellipse correspond approximately to the cross- and in-scan directions. For each source, we projected the IGA position along the major and minor axes of the error ellipse centered at the PSC position. The mean deviations from the PSC position were found to be similar along the major and minor axis directions, and do not scale with the length of the major and minor axes. This indicates the positional errors produced by the MCM algorithm are due to nonsystematic effects unrelated to the *IRAS* scan pattern and detector geometry.

The HIRES algorithm can cause systematic positional shifts if the coverage changes

abruptly. In cases where positional accuracy is important the CVG maps should be checked for the presence of discontinuities or steep ( $< 5'$ ) coverage gradients. The sense of the artifact is to shift source positions systematically down and along the coverage gradient.

#### 4.6. Surface Brightness Accuracy

To test the surface brightness of zodiacal-subtracted IGA images, they were rebinned to match the ISSA geometry (using boxcar averaging) and compared pixel-by-pixel against the ISSA images. The AC/DC correction was applied, i.e. the IGA surface brightness multiplied by 0.92 and 1.0 at 60 and 100  $\mu\text{m}$ , respectively, before calculating the surface brightness correlation (see Section 4.3). The standard deviation of the  $1.5'$  pixel-by-pixel difference is less than 6% for IGA(1) vs. ISSA, and less than 12% for IGA(20) vs. ISSA (see Table 5). The difference is larger at 20th iteration as the rebinned IGA(20) images are still sharper than ISSA, while the 1st iteration IGA images have a resolution similar to the  $4'$  to  $5'$  of ISSA. No systematic offset was found between the IGA and ISSA data (Paper I).

Fig. 7 shows typical scatter plots of  $\log \text{IGA/ISSA}$  vs. ISSA intensities.

#### 4.7. Mosaic Property

The geometry of the IGA images allows them to be mosaicked without any reprojection, hence no smoothing is required and the original resolution can be retained in the mosaicked images. To reduce edge discontinuities, the images should first be cropped to  $1^\circ \times 1^\circ$  from  $1.4^\circ \times 1.4^\circ$  with the centers unshifted before mosaicking. No offset needs to be applied to the different subfields. In most cases the mosaicked image is seamless to the human eye.

Quantitatively, within a chosen Level 1 plate in the W3-5 region, pixel intensity ratios were calculated for 1-pixel wide edges covered by neighboring subfields after cropping the subfields to slightly larger than  $1^\circ \times 1^\circ$ . Table 6 summarizes the intensity ratio statistics for both the 1st and 20th iteration images.

A total of 10122 pixels in 42  $1^\circ$  edges were used in the calculation. For 20th iteration images, the standard deviation of the ratio amounts to 0.51% and 0.23% for band 3 (60  $\mu\text{m}$ ) and 4 (100  $\mu\text{m}$ ) respectively.

Intensity ratio statistics were also calculated for cross-Level 1-plate boundaries, using a total of 8194 pixels in 34  $1^\circ$  edges. Again for 20th iteration images, the standard deviations are 1.5% and 0.46% for band 3 and 4. The match is worse than that of intra-plate edges,

since the zodiacal subtraction was done separately for each Level 1 plate (see Section 3.3).

The better boundary match (smaller deviation) at band 4 can be understood from the poorer resolving power of HIRES at band 4 than at band 3, which decreases the resolution difference between subfields caused by the different flux bias levels used in the image reconstruction process (see Section 3.5).

#### 4.8. Residual Hysteresis

The *IRAS* detectors showed photon induced responsivity enhancement, known as the hysteresis effect, especially in the 60 and 100  $\mu\text{m}$  bands. The effect is prominent when the scan lines pass the Galactic plane (e.g. *IRAS* Catalogs and Atlases: Explanatory Supplement 1988, Chap. VI) and thus a concern for the IGA survey. The final *IRAS* Pass 3 calibration, on which both the IGA and ISSA are based, employed a physically based detector model to correct for the hysteresis. However the technique could not correct variations that were more rapid than  $\sim 6^\circ$  in spatial scale (Wheelock et al. 1994, Chap. III). This section quantifies the residual hysteresis near the Galactic plane in the ISSA data, which should also describe the residual hysteresis present in the IGA.

In the *IRAS* survey, a given region can be covered by up to 3 scans carried out at different times, known as Hours CONfirming (HCON) scans. HCON 1 and HCON 2 were separated by up to several weeks, while HCON 3 was taken roughly 6 months later.<sup>2</sup> This meant HCON 3 usually passed the Galactic plane along the opposite direction of HCON 1 and 2, since *IRAS* followed a Sun-synchronous orbit and the telescope always pointed approximately  $90^\circ$  away from the Sun.

Figure 8 illustrates the effect on quoted flux values from the different HCONs caused by the photon induced responsivity change. At the starting and ending points of a scan, *IRAS* detectors were lit up by an internal flash, which determined the responsivity of the detectors at these two points. In the early calibration schemes, a linear interpolation of the responsivity was done between the two points, and assumed to represent the responsivity change, which is clearly discrepant from the actual effect when the scan passes through bright regions like the Galactic plane (Fig. 8a). Figure 8b illustrates the resulting deviation of quoted fluxes from true values, while Figure 8c shows the variation of the flux ratio of fluxes obtained on descending and ascending scans.

---

<sup>2</sup>Most (96%) of the sky was covered by at least two HCONs, and 2/3 of the sky was covered by three HCONs.



To quantify the residual hysteresis effect in the ISSA images ISSA images made from HCON 1 and 3 were compared at  $l = 0^\circ, 10^\circ, 20^\circ, 60^\circ, 120^\circ, 180^\circ, 240^\circ, 300^\circ, 340^\circ$ , and  $350^\circ$ . Images covering  $\pm 5^\circ$  latitude and  $\pm 2.5^\circ$  longitude were first smoothed with a  $4.5'$  boxcar kernel, roughly the ISSA resolution, and then summed over  $5^\circ$  longitude intervals to increase signal to noise. Pixel intensity ratios (HCON 1 / HCON 3) were computed then averaged over each  $5^\circ (l) \times 4.5' (b)$  box.

Figures 9 and 10 plot the average intensity (left column) and HCON1/HCON3 ratio (right column) versus galactic latitude. Plots made versus galactic latitude are sufficient for our purpose, although strictly speaking ecliptic latitude better represents the *IRAS* scanning direction. The hysteresis signature is seen clearly near  $l = 0^\circ$  with an amplitude of about 20% at  $100 \mu\text{m}$ . As expected, the peak of the average intensity plot corresponds to the appearance of the hysteresis signature in the ratio plot. Hysteresis may also be present in the  $l = 60^\circ$  and  $300^\circ$  graphs but below the 5% level. Other small ( $< 5\%$ ) but systematic variations in the ISSA ratio are likely due to destriping differences. Figure 11 shows the maximum and minimum HCON1/HCON3 ratio found at each longitude. At  $100 \mu\text{m}$  and within  $60^\circ$  of the galactic center, residual hysteresis becomes larger than systematic differences due to destriping and noise.

## 5. Artifacts

For general descriptions on artifacts produced by HIRES processing, see [http://www.ipac.caltech.edu/ipac/iras/hires\\_artifacts.html](http://www.ipac.caltech.edu/ipac/iras/hires_artifacts.html).

### 5.1. Striping Artifacts

Stripes were formerly the most prominent artifacts in HIRES images. HIRES takes as input the *IRAS* detector data, and if not perfectly calibrated, would try to fit the gain differences in the detector scans by a striped image. The striping builds up in amplitude and sharpness along with the HIRES iterations, as the algorithm refines the “resolution” of the stripes.

An algorithm was developed to eliminate the striping artifacts. The basic technique involved is to estimate gain variations in the detectors and compensate for them within the image reconstruction process. Observation of the Fourier power spectrum of resulting images shows that the algorithm eliminates the striping signal after roughly ten iterations. Therefore striping artifacts have been virtually eliminated from the IGA images. See

Paper I for details and examples.

## 5.2. Ringing Artifacts

“Ringing” is a prominent artifact in the IGA images. When a point source is superimposed on a non-zero background, the artifact known as *ringing* or ripples appears in many image reconstruction algorithms. In Fourier language, the reconstruction process tries to make the image agree with the true scene in the low spatial frequency components (data constraint), without access to the infinitely high spatial frequencies inherent in the point source scene.

The magnitude of the ringing depends on the strength of the point source, the level of residual background intensity (after the application of flux bias), and the detector scan pattern. For nonlinear algorithms (such as MCM) the dependence is complicated and difficult to quantify.

The ringing artifact adds uncertainty to the level of background emission around point sources, thus hinders photometric accuracy (see Section 4.2). The ringing may also interfere with the lower intensity structures present in the background. Numerous approaches have been developed in the field of astronomical image reconstruction to overcome the difficulty (Frieden & Wells 1978, Lucy 1994, Bontekoe et al. 1994).

At the time when IGA image production started, no satisfactory algorithm was found for the purpose of ringing suppression for the atlas (see Paper I) which preserves photometric integrity and does not require extra prior knowledge (such as the positions and fluxes of point sources) as input. Therefore the IGA images were produced with the standard MCM algorithm (plus gain compensation destriping), which has the advantage of proven flux conservation. Ringing thus remains as the only major artifact in the IGA images.

Figure 12 demonstrates the ringing around several point sources. At the 1st iteration, the point sources are poorly resolved and no ringing is seen. At the 20th iteration, low intensity rings (the shape of which is roughly elliptical and determined primarily by the detector response functions) surround the point sources. Further away from the point source, a brighter ring is usually visible.

An iterative algorithm was later developed, which aims to maximize the relative Burg entropy between modeled and measured data (Cao et al. 1996b). The algorithm was run on several test fields, and was found to suppress ringing effectively and give good photometry.

A partial convergence proof has also been found.

### 5.3. Glitches

Glitches are caused by hits on individual detectors by cosmic rays or trapped energetic particles. The IPAC utility LAUNDR passes the flux values in each scan line through two filters, one detecting point sources and one glitches. If the ratio of the power in the point source filter to that in the glitch filter is greater than a certain threshold (default is 1), the phenomenon is taken to be a point source, otherwise a glitch.

In a few regions found by visual inspection, glitches were mistaken as point sources and leaked into the image reconstruction stage. In such cases reprocessing with a higher point source to glitch power threshold in LAUNDR sufficed to eliminate the artifact. However, it is not guaranteed that all such artifacts have been uncovered.

In 1st iteration images, a glitch traces out the shape of a single detector response function, and possesses a different profile from that of a point source (a glitch being narrower than a point source). At 20th iteration, glitch would take a “broken-up” shape, showing structures finer than the physically achievable resolution, as shown in Figure 13, while a point source is usually characterized by the ringing artifact. These differences provide a way to distinguish between real point sources and glitches in the images.

### 5.4. Discontinuities

The ISSA images employed both global and local destriping techniques, and the local destriping left some amount of intensity discrepancy between adjacent ISSA plates (Wheelock et al. 1994).

When reprojecting and mosaicking the ISSA images to the Level 1 geometry (against which the detector data are calibrated and zodiacal emission removed), care was taken to adjust the cropping of neighboring ISSA plates to minimize the discontinuity. In a small number of cases however, some discontinuity remained which eventually affected the final IGA image. The discontinuity is not seen in the 1st iterations, but is sharpened and visible in the 20th. Less than 0.5% of all the  $1.4^\circ \times 1.4^\circ$  subfields are affected by this artifact. Figure 14 shows one instance of the discontinuity across a subfield ( $60 \mu\text{m}$ , 20th iteration). The difference in intensity is approximately 5 MJy/ster.

The different flux bias values used in different  $1.4^\circ \times 1.4^\circ$  fields also affects the

mosaicking property of nearby images, since different resolutions are achieved in the overlap region from the two images. See Section 4.7 for a detailed discussion.

### 5.5. Coverage Artifacts

After the processing of the mini-survey ( $-1.7^\circ < b < 1.7^\circ$ ), it was found the data processing window was too small, causing coverage depletion, and therefore unreliable structure near window boundaries. A border of at least  $5'$  should be cropped from images within the mini-survey. For the extended survey ( $1.3^\circ < |b| < 4.7^\circ$ ), a larger window ( $1.67^\circ \times 1.67^\circ$ ) was used in BrkDet to avoid coverage depletion.

The use of a flux bias (see Section 3.5), to bring the data closer to zero during processing, and thereby increase throughput, was necessary but led to a subtle artifact. The IGA processing subtracted a flux bias from the data corresponding to the first percentile from the flux histogram. Data below the threshold were discarded. This procedure effectively assumes the lower 1% of the data are due to noise in the flux values, which is not always justified. In fields which had structured backgrounds, particularly at  $100\ \mu\text{m}$ , it was found that discarding data resulted in severe coverage depletion at the intensity minimum of an image. All images where the coverage fell below a value of 5 in the coverage map were reprocessed with a smaller flux bias. However problems, such as anomalous structure near the image intensity minimum, may remain. The ancillary CVG map can help diagnose problems associated with inadequate coverage.

## 6. Example Images

To illustrate the image quality of the *IRAS* Galaxy Atlas, mosaics at  $60\ \mu\text{m}$  of a restricted latitude range ( $-1.7^\circ < b < 1.7^\circ$ ) were made for regions between Galactic longitude  $280^\circ$  and  $80^\circ$  (approximately 16% of the total area covered by the atlas), and are shown in Fig. 15, 16, 17, and 18. Most of the emission is from stellar heated dust and shows a wealth of star-forming regions, HII regions, and diffuse infrared cirrus (e.g. Fich & Terebey 1996). Extended Galactic infrared emission, long associated with the Galactic HI layer, is readily apparent as enhanced emission near the midplane (e.g. Terebey & Fich 1986, Sodroski et al. 1989). Each panel covers  $11.5^\circ$  in longitude. The dynamic range is much larger than can be displayed, therefore the stretch is logarithmic, with the range chosen separately for each panel to emphasize the most structure.

The complete set of available images and ancillary maps is illustrated for an individual

$1.4^\circ \times 1.4^\circ$  field near IC 1805 in the second Galactic quadrant. Figure 19 shows the coadded and resolution enhanced images plus beam sample maps. Figure 20 shows the associated diagnostic ancillary maps (see Sec. 2). The source IC 1805, an OB cluster exhibiting strong winds and ionizing radiation, is located near the brightest FIR emission. To the north, a cloud suffering erosion from the IC 1805 cluster appears in the infrared as a cometary shaped arc (Heyer et al. 1996). An HI survey of the region shows that the OB cluster appears to fuel a galactic chimney (Normandeau, Taylor, & Dewdney 1996).

## 7. Summary

The *IRAS* Galaxy Atlas, an atlas of the Galactic plane ( $-4.7^\circ < b < 4.7^\circ$ ) plus the molecular clouds in Orion,  $\rho$  Ophiuchus, and Taurus-Auriga has been produced at 60 and 100  $\mu\text{m}$  from *IRAS* data. The HIRES processor, which incorporates the MCM resolution enhancement algorithm, was ported to the Caltech parallel supercomputers for the CPU intensive task.

At 60  $\mu\text{m}$  the typical resolution is  $2.0' \times 4.7'$  for coadded IGA(1) (iteration = 1) images, and  $1.0' \times 1.7'$  for resolution enhanced IGA(20) images, which compares favorably with the  $50''$  diffraction limit of the *IRAS* telescope and the  $5'$  resolution of the previously released *IRAS* Sky Survey Atlas (ISSA). At 100  $\mu\text{m}$ , where the diffraction limit is  $84''$ , the typical IGA(1) resolution is  $3.8' \times 5.4'$  and IGA(20) resolution is  $1.7' \times 2.2'$ , again compared with the  $5'$  ISSA resolution.

The *IRAS* Galaxy Atlas contains images, beam sample maps to assess local resolution, and ancillary diagnostic maps in FITS format. Field sizes are  $1.4^\circ \times 1.4^\circ$  in the Galactic plane, and  $2.0^\circ \times 2.0^\circ$  in the Orion,  $\rho$  Ophiuchus, and Taurus-Auriga molecular clouds.

Zodiacal emission has been removed from the images. The result is images which are easily mosaicked by simple cropping and contain negligible seams. Stripes in the images, long the limiting artifact of standard HIRES processing, have been eliminated by algorithmic improvements to the destriping procedure. “Ringing” around point sources is the major artifact remaining in the IGA images.

Photometry on the IGA images is accurate to roughly 25%, depending on the wavelength and size scale, while positions agree with the *IRAS* Point Source Catalog to better than  $8''$  standard of deviation.

The *IRAS* Galaxy Atlas, combined with other Galactic plane surveys of similar ( $\sim 1'$ ) resolution, provides a powerful venue for multi-wavelength studies of the interstellar

medium, star formation and large scale structure in our Galaxy.

We are indebted to Ron Beck and Diane Engler who carried out the production and recurring rounds of reprocessing of the *IRAS* Galaxy Atlas. We thank John Fowler for his help with the YORIC software. The project received support from the Astrophysics Data Program of the National Aeronautics and Space Administration under contract No. NAS5-32642. This work was performed in part at the Jet Propulsion Laboratory, California Institute of Technology, under a contract with the National Aeronautics and Space Administration. The atlas production was performed in part using the Intel Paragon operated by Caltech on behalf of the Concurrent Supercomputing Consortium.

## REFERENCES

- Assendorp, R. Bontekoe, T. J. R., Dejonge, A. R. W., Kester, D. J. .M., Roelfsema, P. R., & Wesselius, P R. 1995, A&AS, 110, 395
- Aumann, H. H., Fowler, J. W., & Melnyk, M. 1990, AJ, 99, 1674
- Bontekoe, T. R., Koper, E. & Kester, D. J. M. 1994, A&A, 284, 1037
- Cao, Y., Prince, T. A., Terebey, S., & Beichman, C. A., 1996, PASP, 108, 535
- Cao, Y., Eggermont, P. P. B., & Terebey, S., to be submitted to IEEE Trans. Medical Imaging
- Fich, M., & Terebey, S. 1996, ApJ, to appear Dec 1
- Fowler, J. W. & Aumann, H. H., in *Science with High Spatial Resolution Far-Infrared Data*, Terebey, S. & Mazzarella, J. (eds.) 1994, (Pasadena: JPL 94-5)
- Frieden, B. R. & Wells, D. C. 1978, J. Opt. Soc. Am., 68, 93
- Good, J. C., in *IRAS Sky Survey Atlas Explanatory Supplement*, ed. Wheelock, S. L., Gautier, T. N. et al. 1994, App. G (Pasadena: JPL 94-11)
- Greisen, E. W. & Calabretta, M. 1996, submitted to A&A
- Heyer, M. H. 1996, in “CO: Twenty-Five Years of Millimeter Wave Spectroscopy”, Eds. W. Latter, D. Emerson, & S. Radford

- M.H. Heyer, M. H., Brund, C., Snell, R. L., Howe, J., Schloerb, F. P., Carpenter, J. C., Normandeau, M., Taylor, A. R., Cao, Y., Terebey, S., & Beichman, C. A. 1996, ApJ, 464, L175
- Hurt, R. L., & Barsony, M., ApJ, 460, L45
- IRAS Catalogs and Atlases: Explanatory Supplement* 1988, Beichman, C. A., Neugebauer, G., Habing, H. J., Clegg, P. E., & Chester, T. J. (editors) (Washington D.C.: GPO)
- IRAS Point Source Catalog, Version 2* 1988, Joint *IRAS* Science Working Group (Washington, D.C.: GPO)
- Lucy, L. B., 1974, AJ, 79, 745
- Lucy, L. B. 1994, in “The Restoration of HST Images and Spectra – II”, pp. 79–85 (Baltimore: STScI)
- Rice, W., 1993, AJ, 105(1), 67
- Richardson, W. H., 1972, J. Opt. Soc. Am., 62, 55
- Sodroski, T.J., Dwek, E., Hauser, M.G., & Kerr, F.J. 1989, ApJ, 336, 762
- Surace, J. A., Mazzarella, J. M., Soifer, B. T., & Wehrle, A. E. 1993, AJ, 105, 864
- Normandeau, M., Taylor, A. P. & Dewdney, P. E. 1996, Nature, 380, 687
- Terebey, S., & Fich, M. 1986, ApJ, 309, L73
- Terebey, S. & Mazzarella, J. (eds.) 1994, Science with High Spatial Resolution Far-Infrared Data, (Pasadena: JPL 94-5)
- Wells, D. C., Greisen, E. W. & Harten, R. H., A&AS, 44, 363
- Wheelock, S. L., Gautier, T. N. et al. 1994, *IRAS* Sky Survey Atlas Explanatory Supplement, (Pasadena: JPL 94-11)

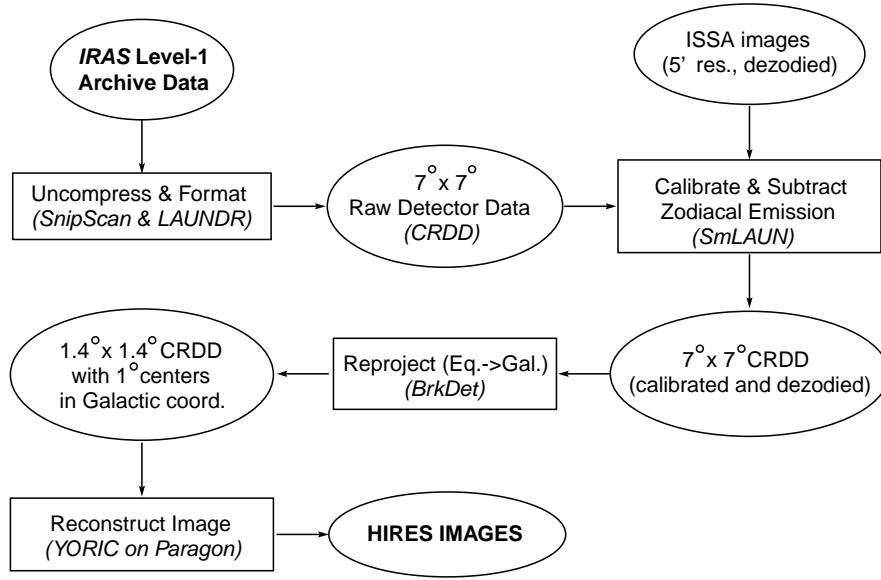


Fig. 1.— Outline of the IGA Production Pipeline



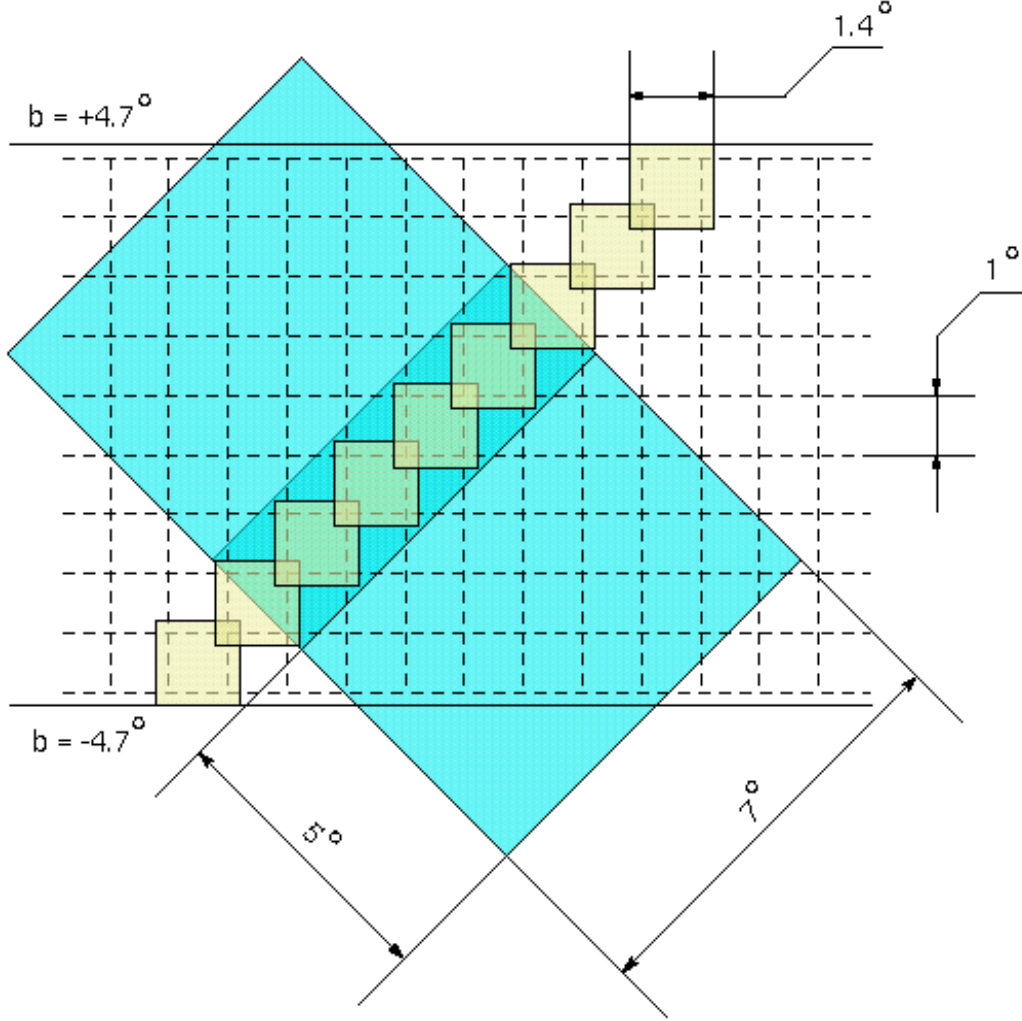


Fig. 2.— Geometry of IGA fields in Galactic coordinates relative to the input Level 1 Plate data in equatorial coordinates). The Atlas covers  $-4.7^\circ < b < 4.7^\circ$ . The small shaded areas represent IGA fields ( $1.4^\circ \times 1.4^\circ$  on  $1^\circ$  centers), while the large ones Level 1 plates ( $7^\circ \times 7^\circ$  on  $5^\circ$  centers). The configuration shows in an extreme case,  $1.4^\circ \times 1.4^\circ$  is the largest IGA field that can be fully covered by any single Level 1 plate.

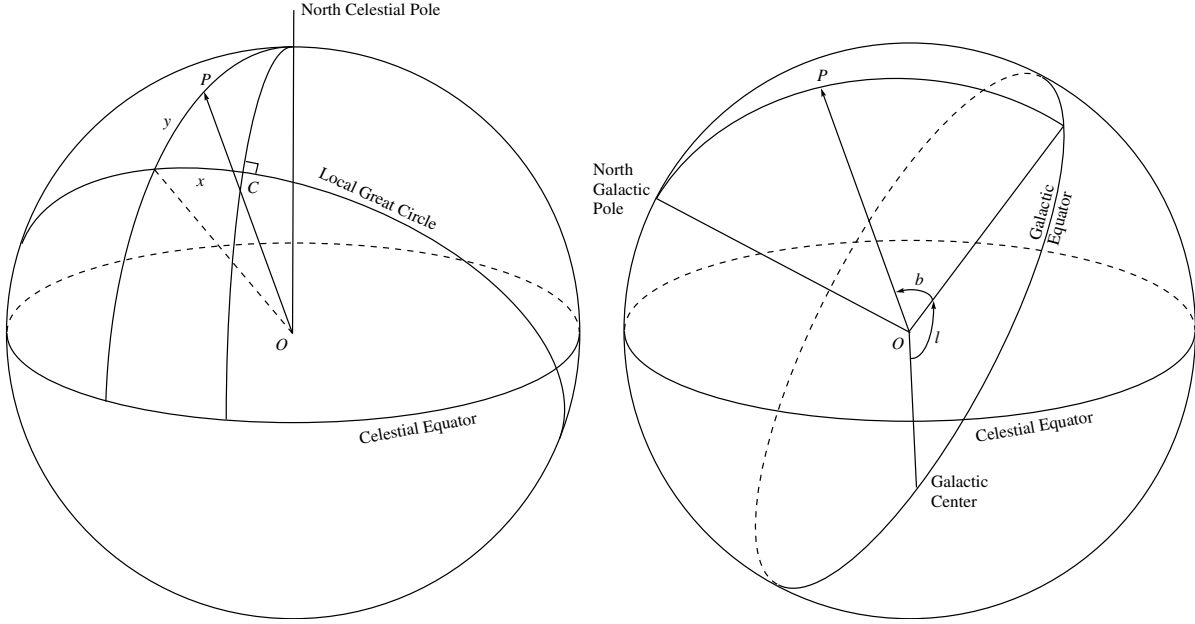


Fig. 3.— Reprojection of Footprint Coordinates. In the diagram on the left, RA and Dec are known for the Level 1 plate center  $C$ , and  $x$  (negative as shown here) and  $y$  are known for the footprint  $P$ . The components of the unit vector  $OP$  is then computed (in equatorial system). As shown on the right, the vector  $OP$  is rotated to Galactic system, from which  $l$  and  $b$  of the footprint are obtained.

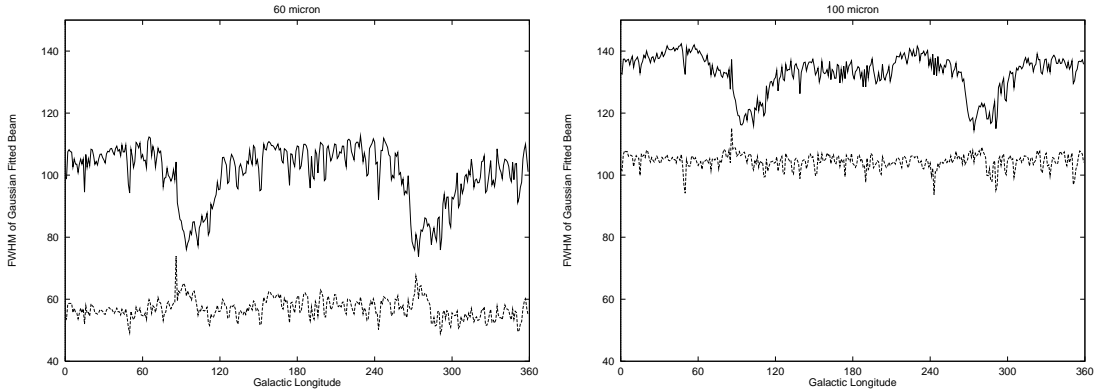


Fig. 4.— Dependence of Beam Size on Galactic Longitude. Left and right plots are for 60 and 100  $\mu\text{m}$  respectively. The top and bottom curves in each figure are the FWHM of Gaussian fitted beam along the major and minor axes respectively. The regions in the Galactic plane which had intersecting scan lines in the *IRAS* survey are seen as two dips in the major axis curves (better resolution due to extra geometrical information).

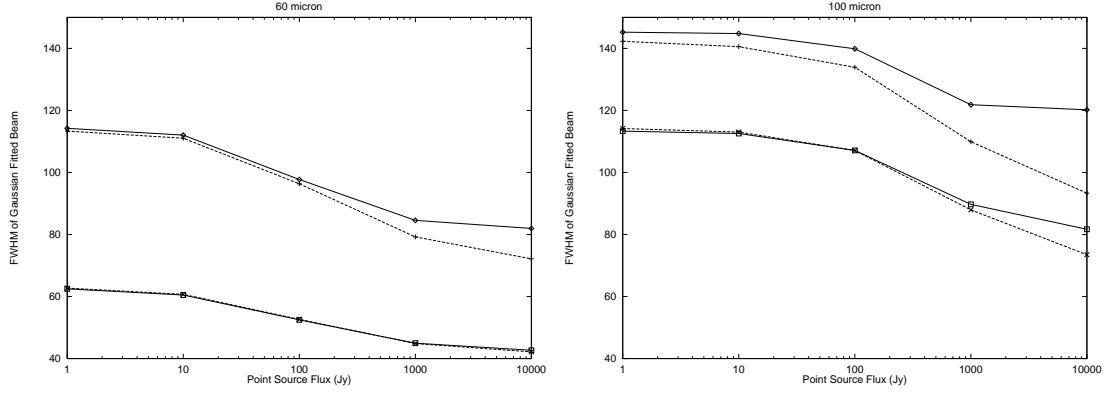


Fig. 5.— Dependence of Beam Size on Source Flux. Resolution significantly improves for sources stronger than the local processing background of 33.7 Jy at 60  $\mu\text{m}$  and 223 Jy at 100  $\mu\text{m}$ . Results with destriping (solid lines), and non-destriping (dashed lines) show the IGA destriper has comparable resolution to standard HIRES, the most notable difference along the 100  $\mu\text{m}$  major axis.

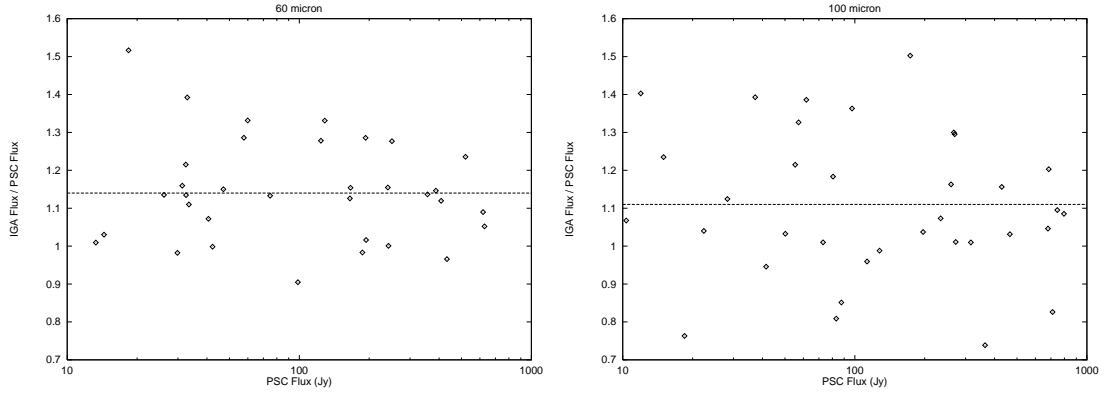


Fig. 6.— The ratio of (IGA(20) Flux / PSC Flux) vs. PSC Flux shows no trend with source strength. Offsets are discussed in text. Thirty-five sources are plotted in each wavelength band.

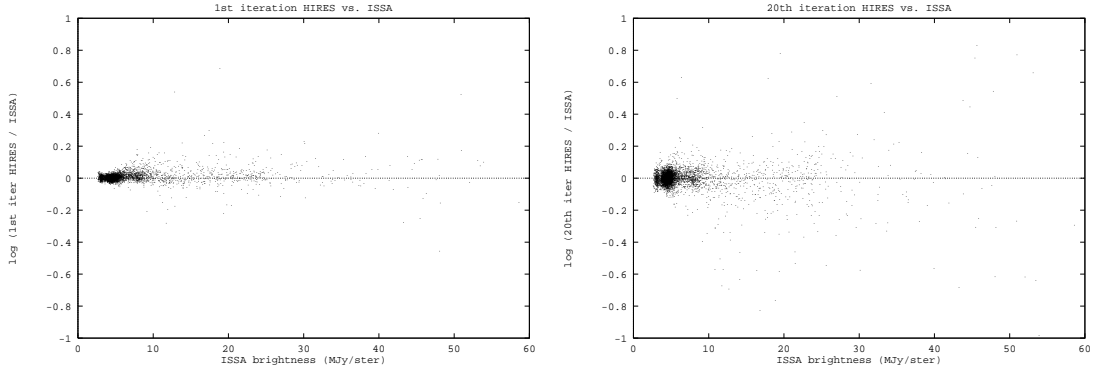


Fig. 7.— Comparison of IGA and ISSA surface brightness in a  $1^\circ$  radius circular area centered at  $g218.5, -0.5$  ( $60 \mu\text{m}$ ) shows no systematic offset. Left: comparison of IGA(1) vs. ISSA; right: comparison of IGA(20) vs. ISSA. Vertical: log of IGA/ISSA ; horizontal: ISSA intensity in MJy/ster. The AC/DC correction was applied before calculating surface brightness ratio. Reprinted from Paper I.

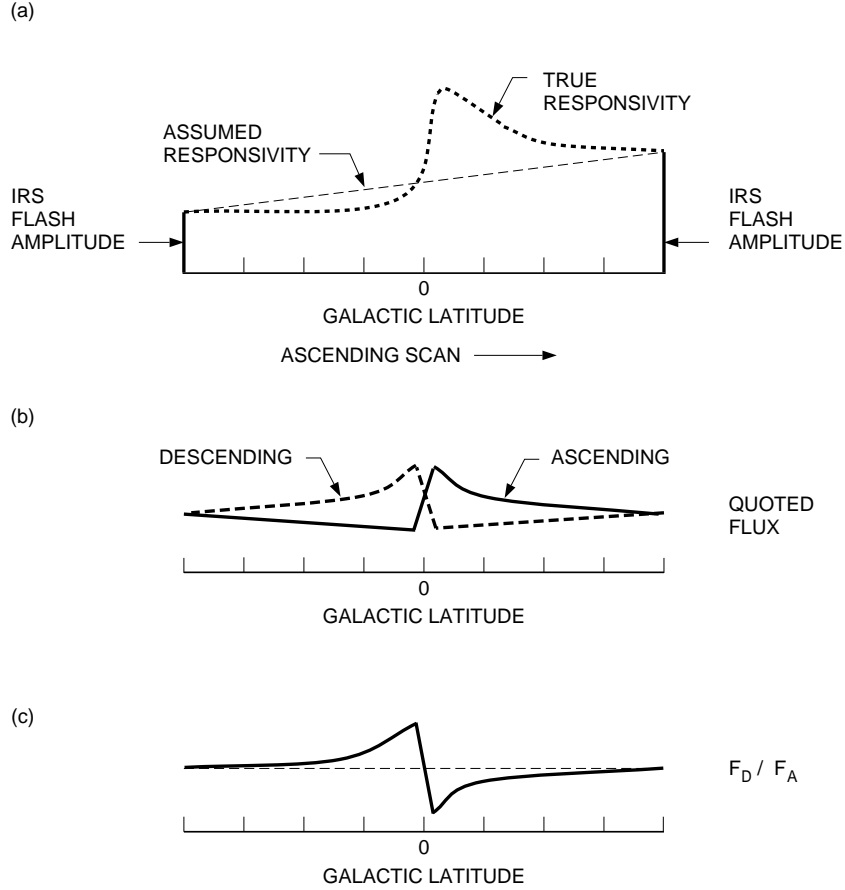


Fig. 8.— Illustrations of the Hysteresis Effect. (a). Internal flashes of known magnitude were used at the starting and ending points of a scanline, in an effort to determine the responsivity change (dashed line, assumed responsivity). The true responsivity is shown in the dashed curve, due to photon induced responsivity enhancement; (b). Quoted fluxes from ascending and descending scans deviate from the true values; (c). The ratio of quoted fluxes varies with Galactic latitude. (Adapted with changes from Figure VI.B.2, *IRAS* Catalogs and Atlases: Explanatory Supplement 1988.)

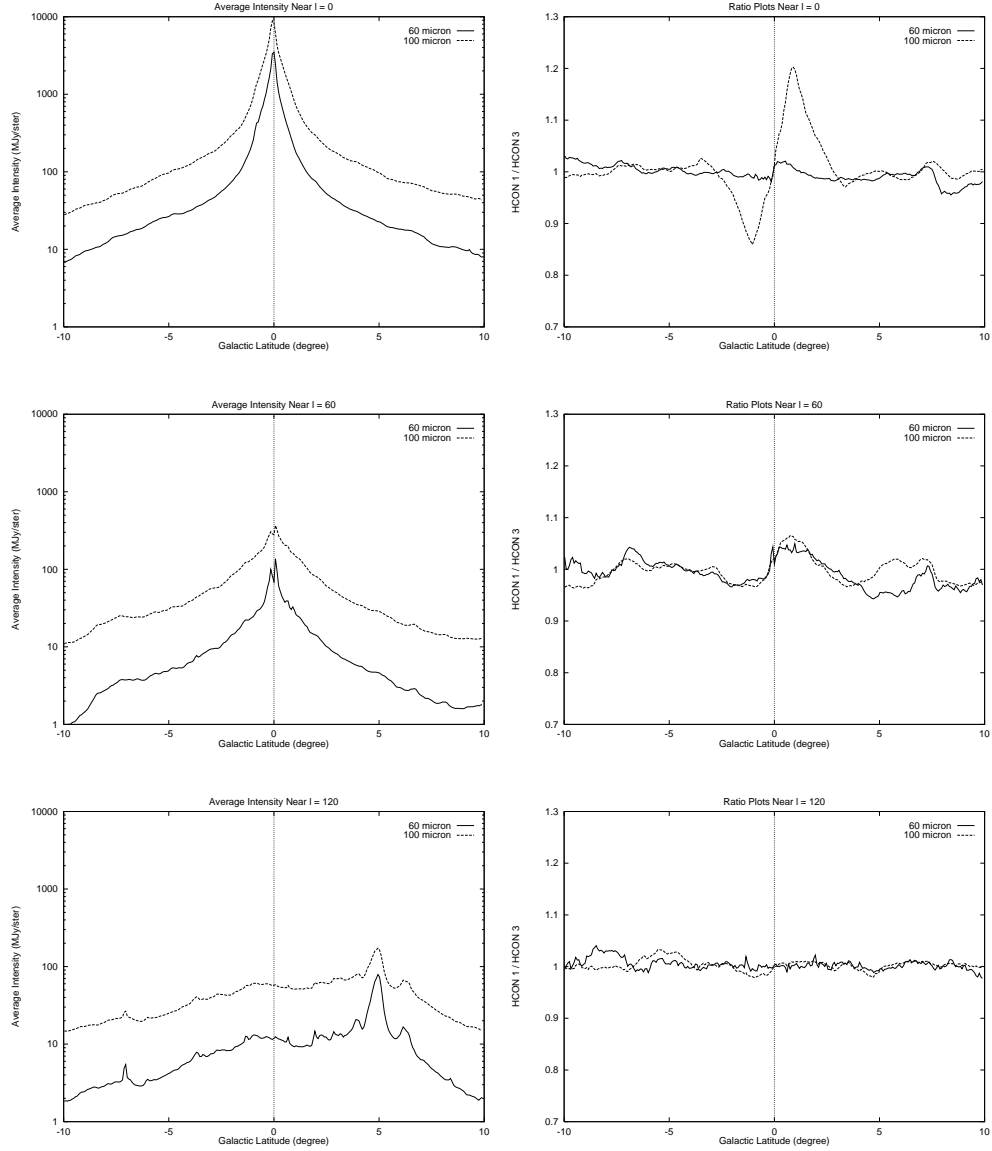


Fig. 9.— Average Intensity and Ratio of ISSA Intensities from Opposite Scans,  $l = 0^\circ$ ,  $60^\circ$ , and  $120^\circ$ . The hysteresis signature is seen clearly near  $l = 0^\circ$  with an amplitude about 20% at  $100 \mu\text{m}$ . Hysteresis may also be present in the  $l = 60^\circ$  and  $300^\circ$  graphs but below the 5% level. Other small ( $< 5\%$ ) but systematic variations in the ISSA ratio are likely due to destripping differences.

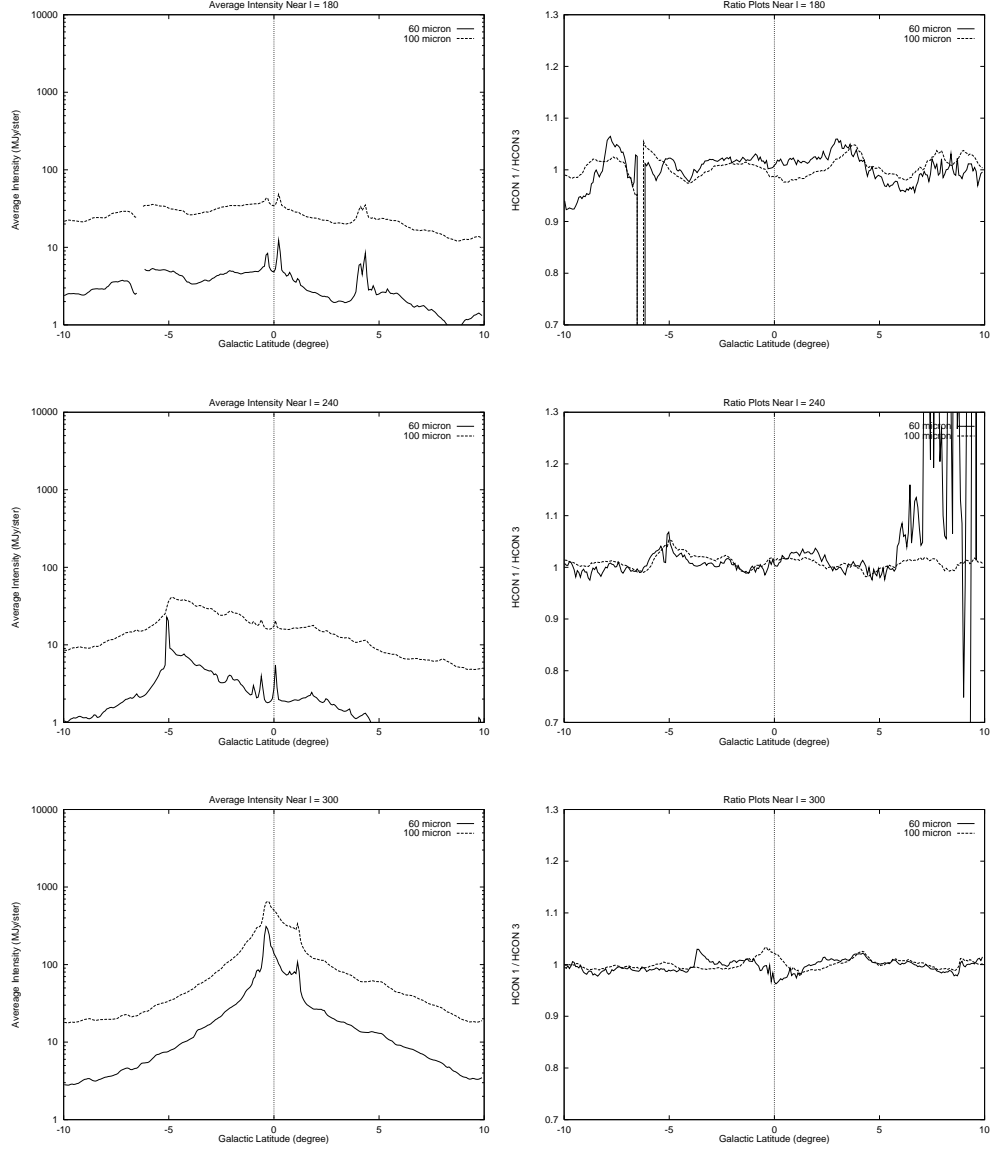


Fig. 10.— Average Intensity and Ratio of ISSA Intensities from Opposite Scans,  $l = 180^\circ$ ,  $240^\circ$ , and  $300^\circ$ .

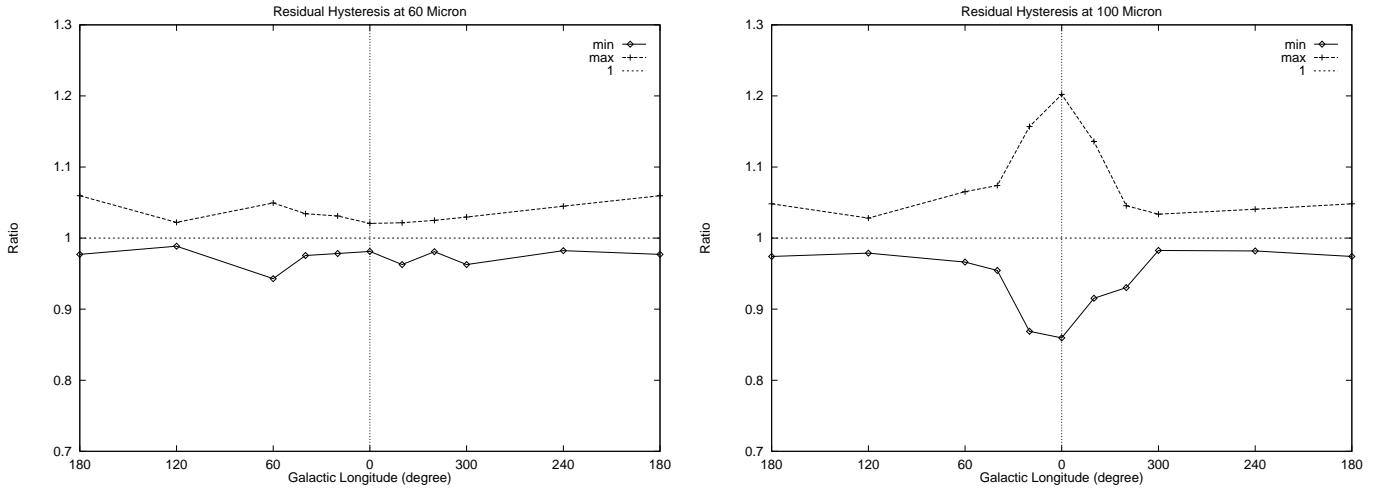


Fig. 11.— Minimum and Maximum Intensity Ratios vs. Galactic Longitude. Left: 60  $\mu\text{m}$ ; Right: 100  $\mu\text{m}$ . At 100  $\mu\text{m}$  and within 60° of the galactic center, residual hysteresis becomes larger than systematic differences due to destripping and noise.



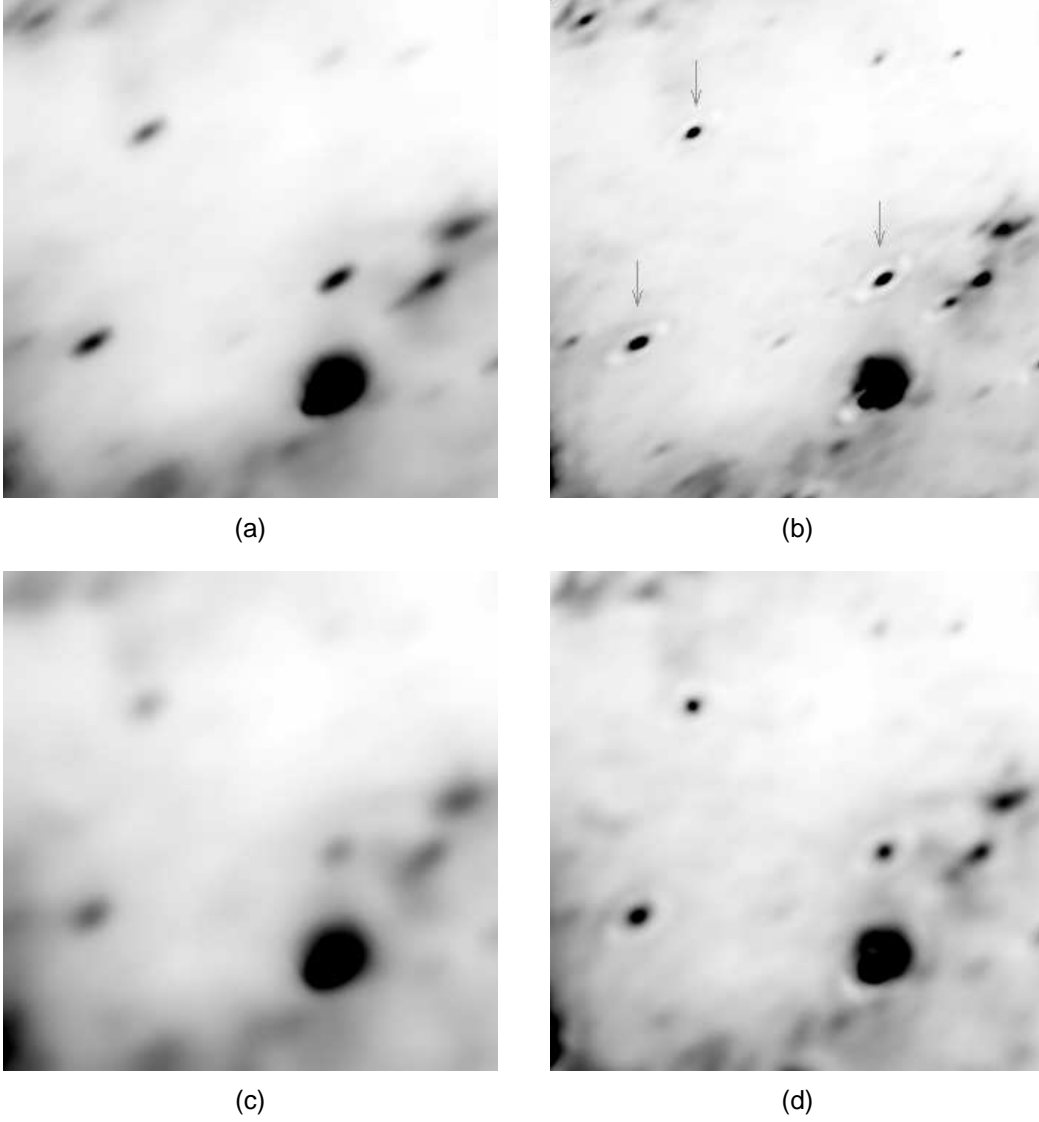


Fig. 12.— Demonstration of the Ringing Artifact. (a). 1st iteration, 60  $\mu\text{m}$ ; (b). 20th iteration, 60  $\mu\text{m}$ ; (c). 1st iteration, 100  $\mu\text{m}$ ; (d). 20th iteration, 100  $\mu\text{m}$ . Ringing is not seen for the 1st iteration images, but is prominent in the 20th. Field center is at  $l = 75^\circ, b = 1^\circ$ ; field size is  $1.4^\circ$  on each side. Black is brighter in the images.

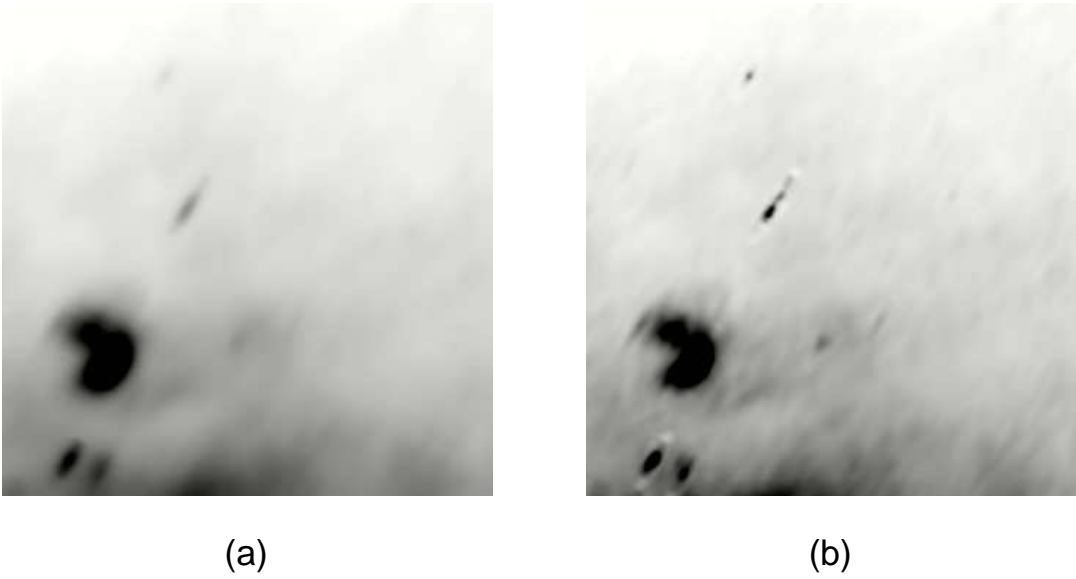


Fig. 13.— Demonstration of the Glitch Artifact. The elongated feature to the upper-left of the field center is a glitch. (a) and (b) show the glitch at 1st and 20th iteration respectively. At 20th iteration, the glitch takes a “broken-up” shape. Black is brighter in the images. Field center is  $l = 7^\circ, b = 1^\circ$ , field size is  $1.4^\circ$  on each side.



Fig. 14.— Discontinuity Across One Subfield.  $60\ \mu\text{m}$ , 20th iteration, field center is  $l = 48^\circ, b = 1^\circ$ ,  $1.4^\circ$  on each side. The difference in intensity is approximately 5 MJy/ster.

Fig. 15.— *IRAS* Galaxy Atlas images of the Galactic plane at  $60\ \mu\text{m}$ , Longitude  $0^\circ - 40^\circ$  show a variety of star-forming regions, HII regions, and the diffuse IR emission associated with the Galactic HI layer. Each panel covers  $11.5^\circ$  in longitude and  $-1.7^\circ < b < 1.7^\circ$  in latitude, with logarithmic stretch chosen to emphasize structure.

Fig. 16.— The Galactic Plane at  $60\ \mu\text{m}$ , Longitude  $40^\circ - 80^\circ$ .

Fig. 17.— The Galactic Plane at  $60\ \mu\text{m}$ , Longitude  $280^\circ - 320^\circ$ .

Fig. 18.— The Galactic Plane at  $60\ \mu\text{m}$ , Longitude  $320^\circ - 0^\circ$ .

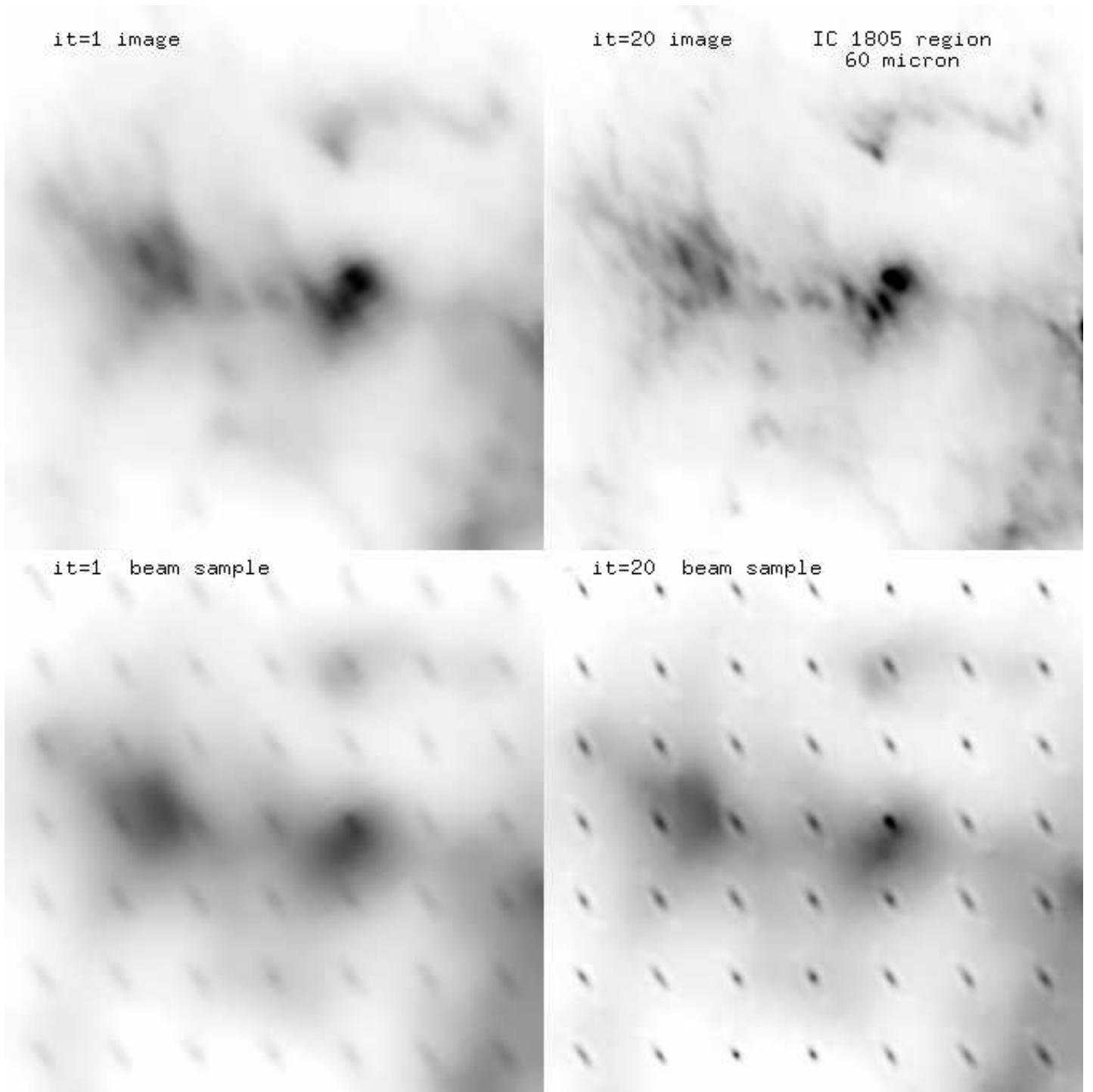


Fig. 19.— Example  $1.4^\circ \times 1.4^\circ$  *IRAS* Galaxy Atlas images plus beam sample maps near the IC1805 OB cluster.

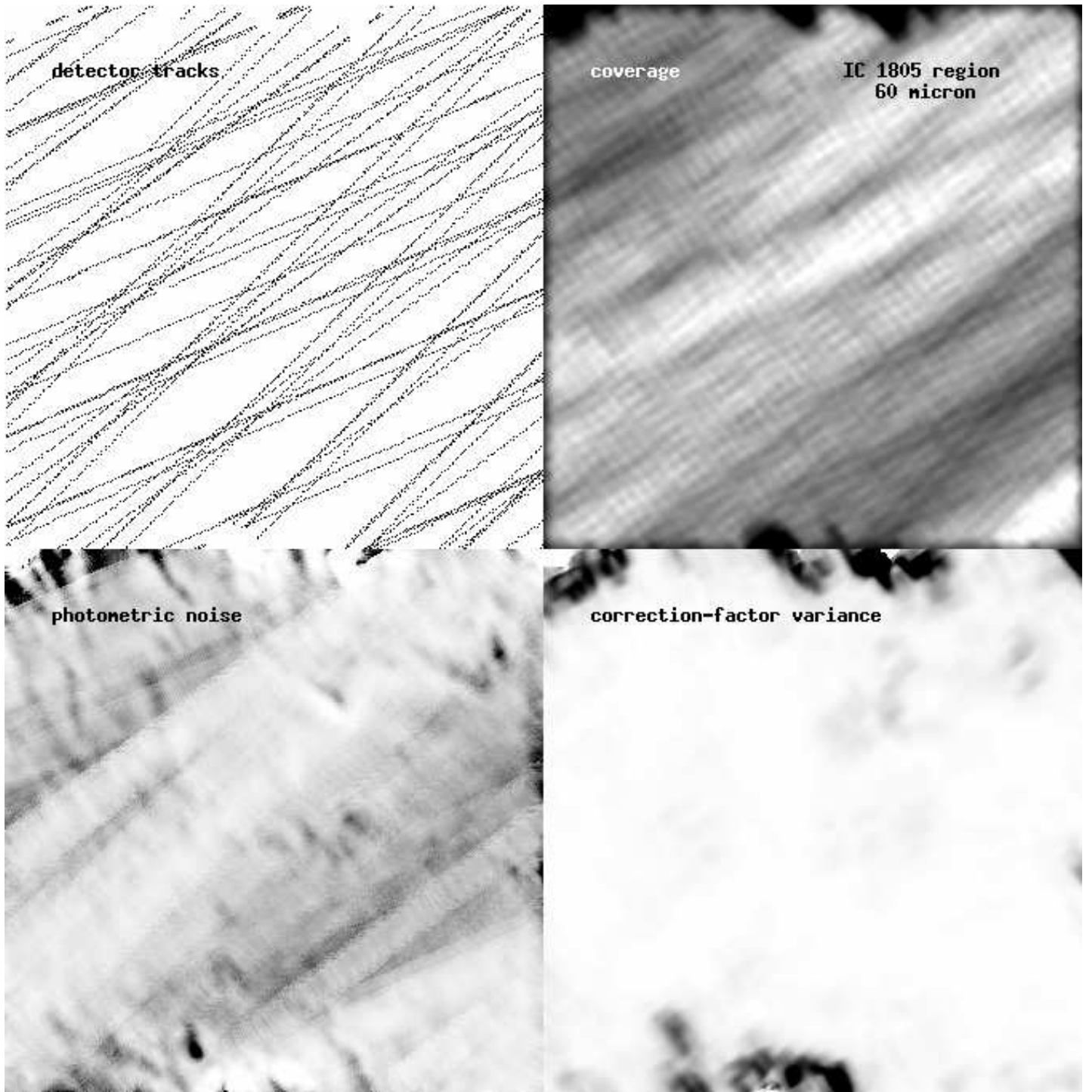


Fig. 20.— Examples of diagnostic ancillary maps for field near the IC1805 OB cluster.

